Article

Functionalized Bacteriophages Silk Fibroin-Based Films with Antimicrobial Potential

Tolbert Osire , Yueqi Wang , Guojing Lu , Liubov Popova , Olga Burtseva , Evgeniya Yu. Parshina , Olga S Sokolova *

Posted Date: 18 December 2023

doi: 10.20944/preprints202312.1238.v1

Keywords: bacteriophage AR9; Bacillis subtilis; silk fibroin scaffolds; Raman spectroscopy; SEM

Article

Functionalized Bacteriophages Silk Fibroin-Based Films with Antimicrobial Potential

Tolbert Osire [1], Yueqi Wang [1], Guojing Lu [1], Liubov Popova [1], Olga Burtseva [1], Evgeniya Yu. Parshina [1,2]and Olga S Sokolova [1,2]

[1] Faculty of Biology, Shenzhen MSU-BIT University, 1 International University Park Road, Shenzhen, 518172, China; ljubovprokudina@gmail.com, (LP); 6420210017@smbu.edu.cn, (TO); 3120210002@smbu.edu.cn, (YW); 6420190025@smbu.edu.cn, (GL); 6620160006@smbu.edu.cn, (OB)

[2] Faculty of Biology, Moscow Lomonosov University, 1 Leninskie gory, bld 12, Moscow, 119234, Russia; parshinae@gmail.com, (EYP)

* Correspondence: sokolova_o@smbu.edu.cn;

Abstract: Scaffolds used for tissue/ bone defect repair must possess versatile properties suitable for each specific application. The issue of antibiotic resistance poses a significant challenge in bone tissue engineering especially when dealing with microbial infections. The most effective approach to address this challenge is to promote the integration of tissue before bacteria can adhere to it, hence preventing the proliferation of certain bacterial strains on the implant. The utilization of 3D printing and or the use of various composite polymers in scaffolds to create antibacterial scaffolds that possess both adequate mechanical strength and exceptional biocompatibility is an attractive approach for addressing the challenges associated with microbial infections in tissue. Herein, a new phage functionalized scaffold was created through surface charge modification of the composite scaffold with polyethyleimine (PEI). Afterwards, the PEI polymerized Scaffolds were incubated with phage lysate for approximately 2h prior to rinsing with ethanol. The morphological and physiochemical properties of formed scaffold were assessed through Raman spectrophotometry while the antibacterial assays were done through growth inhibition zones/ cell viability assays. The polymerized phage composite SF20_PEI.AR9 possessed the highest antimicrobial effect with clear inhibition zones of about 78.30 mm. This could be attributed to the lytic effect of phages on the bacterial cells. Moreover, the enhanced phage effect on the scaffolds was also associated to the improved surface charge on the scaffold, 78,3±7,6 mm which ultimately promoted phage scaffold interface integration hence the high antibacterial activity. The PEI polymerization approach could serve as a model for future development of phage scaffolds.

Keywords: bacteriophage AR9; *Bacillis subtilis*; silk fibroin scaffolds; Raman spectroscopy; SEM

1. Introduction

The primary obstacles encountered in the development of robust biomaterials for broad applications, encompass the development of advanced matrix architectures that provide efficient distribution of oxygen and nutrients vital in tissue engineering [1], promote early and selective detection of pathogens in food safety biosensors [2]. In essence, the designed biomaterial should possess a porous structure, which could permit the influx of low molecular weight solutes, oxygen and nutrients essential for cell viability, as well as the efflux of wastes from the scaffolds [3]. Moreover, to mimic natural systems, where molecular affinity and subsequent substrate specificity by biological molecules, play a crucial role in facilitating the organization of fundamental building blocks into hierarchical structures, the integration of biological components (bacteria, phages and biological molecules) into the scaffolds could facilitate emergence of innovative biomaterials with unlimited capabilities for broad applications [4].

Bacterial residues attached on surfaces such as injured tissues, equipment, pipelines, and packaging are a major cause of contamination, leading to illnesses and financial losses, with the economic impact of foodborne illnesses predicted at about US$90 billion [5], while the pre-COVID-19 pandemic estimates from 2019 indicated that biofilms hold significant economic impact,

 doi:10.20944/preprints202312.1238.v1

surpassing $5000 billion yearly [6]. To combat microbial infections, various pharmaceutical remedies such as antibiotics have been employed to combat microbial infections. However, their extensive use has resulted in emergence of highly resistant strains, commonly referred to as superbugs, posing a threat to human health [7-9]. Consequently, there exists an urgent need to develop novel biomaterials for early detection of pathogens as well as new antibacterial materials.

Over the past decades, significant attention has been directed towards the advancement of several types of biomaterials, including antimicrobial scaffolds, with the aim of achieving rapid, sensitive, and specific detection and efficient elimination of pathogens [10-13]. The potential of antimicrobial peptides to serve as next-generation antibiotics has also garnered significant interest among researchers, mostly owing to their favorable attributes such as biosafety, degradability, and capacity to disrupt the cell membranes of pathogens [14]. Nevertheless, the utilization of costly nucleic acid, bacterial, and enzyme-based probes/ biomaterials that are sensitive to temperature, pH, and environmental conditions, imposes constraints on their broad practical application [2].

Bacteriophages exhibit a high degree of specificity/selectivity, are cost-effective to produce at high titers and demonstrate tolerance to variations in pH and temperature within the growing medium, thus the utilization of phage-based biomaterials presents effective alternatives for engineering of new biomaterials [15,16]. To utilize bacteriophages as bio-probes or antimicrobials with enhanced overall efficacy, it is essential to immobilize them on suitable substrates at substantially high quantity [2]. This has been accomplished through direct physical adsorption [17], chemical/ covalent immobilization [18,19], genetic engineering [20], encapsulation [21,22], and self-assembly [22,23]. Several materials have been used as substrates for immobilization of bacteriophages. For example, Roy et al. through phage biopanning displayed functional peptides for bone regeneration on Hydroxyapatite (HAP) scaffolds [24], Jin et al. applied Palladium (Pd) nanozyme-armed phage as a versatile antibacterial solution [25], Singh et al. immobilized bacteriophages on gold surfaces to facilitate the targeted capture of pathogens [26] while Konwarh et al. made a biopolymer from ultrafine cellulose fibres for application as membranes, bandages, among others [27].

Silk fibroin (SF) has garnered considerable attention in the field of material science due to its biocompatibility, biodegradability, and exceptional mechanical qualities, as well as its simplicity of modification [28]. For example, Eivazzadeh-Keihan et al. fabricated a nanobiocomposite scaffold with antimicrobial activity and improved mechanical properties by cross-linking a chitosan-based hydrogel with SF [29].

Here we developed a phage-functionalized scaffold with antibacterial potential by surface modification of the silk fibroin-based scaffold through polymerizing with the highly charged Polyethyleneimine (PEI). We assessed the antibacterial activity of the SF based scaffolds and analyzed their morphology, structural and functional group properties by spectral and analytical techniques such as SEM, FT-IR, and Raman spectrophotometry. Thus, polymerization of scaffolds with PEI may be useful for the future development of antibacterial scaffolds.

2. Results

2.1. Production of Phage Functionalized SF Blends

The ultimate goal of this study was to develop a silk fibroin/phage-based scaffold with antibacterial activity. The 3D SF scaffold was thus developed through direct mixing and freezing approach and later the formed scaffold was surface modified with polymerized with polyethyleimine (PEI) to introduce positive charges on the scaffold (Fig.1). The highly porous and super fibrous network structure SF composite allowed for the impregnation of the scaffolds with PEI, hence imparting the desired properties to the scaffold. Ultimately, the phage particles are immobilized in the scaffold matrix through electrostatic interactions between the PEI-modified positively charged scaffold fibers interacting with the negative charges of the phage head. Therefore, the polymerization with PEI, an amine-rich polycation, serves as a reducing agent in the synthesis of the SF_PEI composite as well as a binding agent for binding to the anionic phage head.

Preprints (www.preprints.org) | NOT PEER-REVIEWED | Posted: 18 December 2023 doi:10.20944/preprints202312.1238.v1

Moreover, there could be other potential chemical interactions during PEI polymerization such as hydrogen bond interactions between amino groups from PEI with –COOH groups of SF protein as well as possible interactions between the phage head protein amino acid side groups, such as –COOH and C–C groups with the PEI-functionalized scaffold.

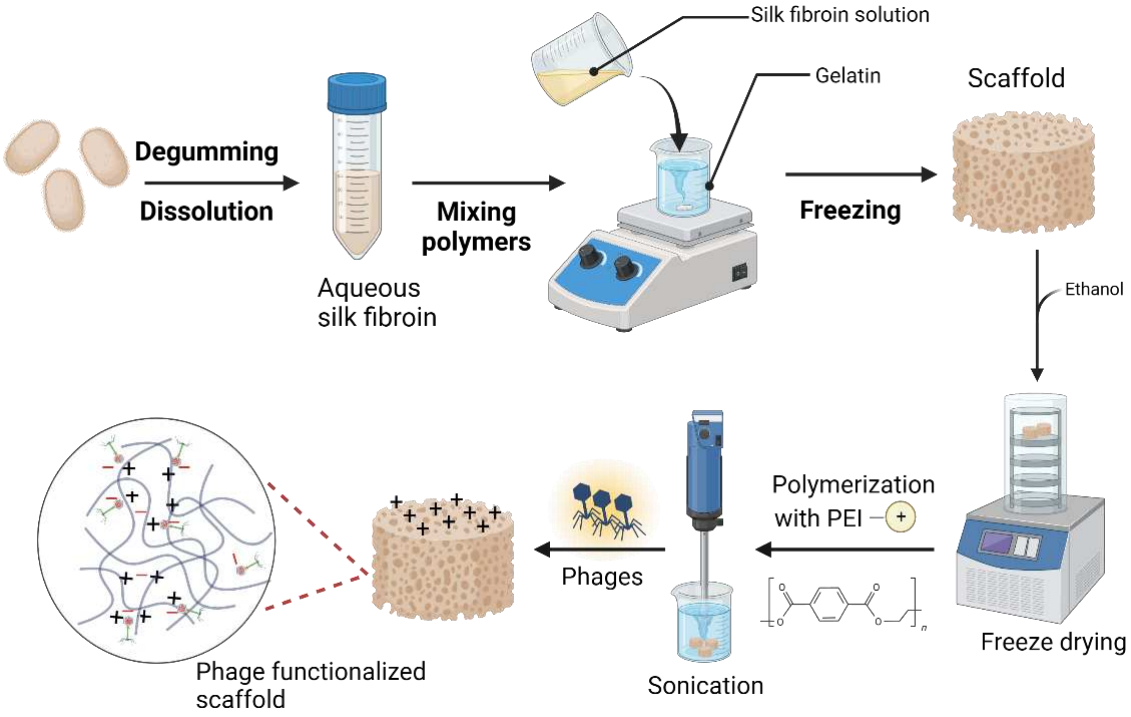

Figure 1. Outline of the stepwise production process and functionalization of the silk fibroin-based scaffolds (prepared with Biorender).

2.2. SEM Structural Analysis of the Scaffolds

Diameter distribution and pore morphological properties of SF20 and SF20_PEI composite scaffolds were determined through SEM. The SEM micrographs showed that the scaffolds possessed fine fiber architecture consisting of a porous 3D network- arrangement (Fig.2 a) composed of loosely arranged fibres, ranging in size from 80 μm to 1000 μm diameter. Notably, polymerization with PEI resulted in overall reduction of the pore sizes. However, for the pore size distribution, the SF20 and SF20_PEI composite scaffolds possessed approximately 47.90 % and 41.06 % pores ranging in size between 0-200 μm, with a porosity of 68.92 % and 77.27 %, respectively (Fig.2 b).

Preprints (www.preprints.org) | NOT PEER-REVIEWED | Posted: 18 December 2023 doi:10.20944/preprints202312.1238.v1

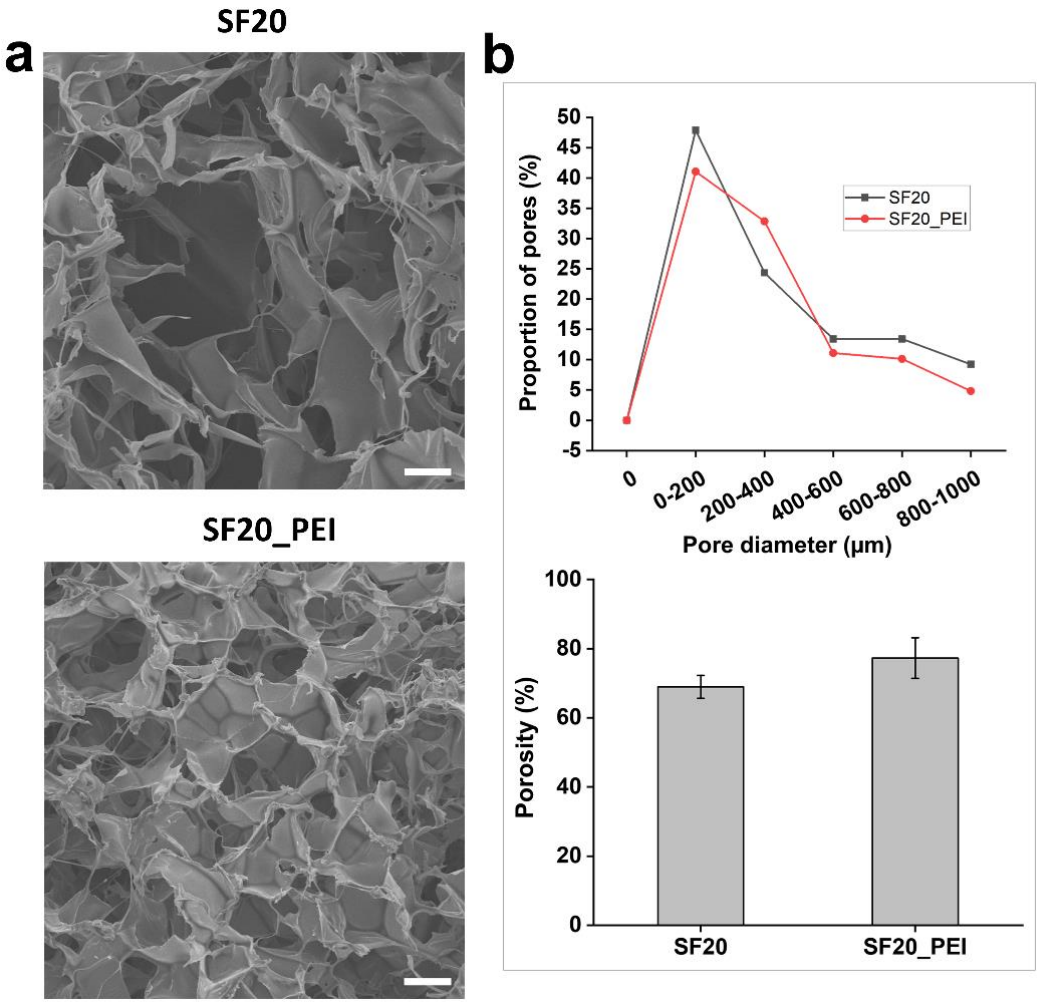

Figure 2. SEM micrographs, pore size distribution and porosity of the SF20 and SF20_PEI polymerized scaffolds. a. the porous structure of SF20 SF20_PEI scaffolds. b. pore size distribution (Top) and porosity of the SF20 SF20_PEI scaffolds, respectively. Bar size - 150 um.

2.3. In Vitro Swelling Rate and Water Solubility of the Scaffolds

Typically, the swelling rate of biomaterials is closely associated with the permeability of the material, which in turn plays a crucial role in the transportation of nutrients and waste in and out of the scaffold. It has also been reported to influence cell adhesion and proliferation on the scaffold material [30]. As shown in Table 1,all the scaffolds had high swelling rates above 85%. Specifically, the SF20 scaffold had the highest swelling rate of about 96.61%, SF20.AR9 scaffold possessed 94.49 %, while SF20_PEI.AR9 had the lowest swelling rate of swelling rate of about 86.55%. The high rate of swelling in the SF20 scaffold could be associated with the large pore sizes in this scaffold, while the polymerization of the original scaffold with PEI resulted in a reduced swelling rate. Firstly, this observation could be due to the reduction in pore sizes which thus permit less water into the scaffold. Secondly, the polymerization effect results in formation of a dense network of fibers, which limit hydration (entry of water). Although scaffold SF20_PEI.AR9 had been polymerized, introduction of phages into this scaffold could attributed to its low swelling rate. It is a well-known phenomenon that phages have the ability to interact with charged biomaterial surface thus forming crosslinks, which ultimately restrict the rate of swelling rates.

The water solubility of scaffolds can serve as an indicator for the stability or water-resistance of the scaffolds, which is a crucial for application. Table 1 showed that the water solubility of the SF20 scaffold was highest at 67.10, while that of non-polymerized scaffold SF20.AR9 (with phage) was 52.91%. However, the PEI polymerized scaffolds both had low water solubility with the SF20_PEI

Preprints (www.preprints.org) | NOT PEER-REVIEWED | Posted: 18 December 2023 doi:10.20944/preprints202312.1238.v1

scaffold having the lowest water solubility followed by SF20_PEI.AR9. This observation could be associated to the formation of bond interactions between the scaffold surface and or with the phages, hence improving scaffold integrity.

Table 1. The water uptake, swelling and degradation of the SF-based scaffolds.

Scaffold Type	Swelling rate (%)	Water solubility (%)
SF20	96.61	67.10
SF20_PEI	91.37	35.75
SF20.AR9	94.49	52.91
SF20_PEI.AR9	86.55	41.53

2.4. In Vitro Degradation of the Composite Scaffolds

In vivo, tissue engineering scaffolds serve as a temporal platform for cell proliferation attachment, growth and distribution and therefore tunable scaffold degradation is of paramount significance for the development and application of biomaterials, as its essential for the sustained regeneration of new tissue structure [31,32]. We assessed the degradation behavior of the SF based scaffolds in PBS as well as under mild alkaline (Sodium hydroxide) conditions at 37 ℃ at different time intervals up to 2 weeks. Generally, the degradation effect on all scaffolds in 0.01M PBS buffer was slow and there was no significant degradation even after 2 weeks incubation (data not shown). Comparatively, as shown in Fig.3, under 0.1M sodium hydroxide solution, the rate of degradation of the scaffolds was very fast. Specifically, the percentage weight loss, although varying to a large extent for all the scaffold types was significantly increased and nearly reached 100% within the 10 h of incubation.

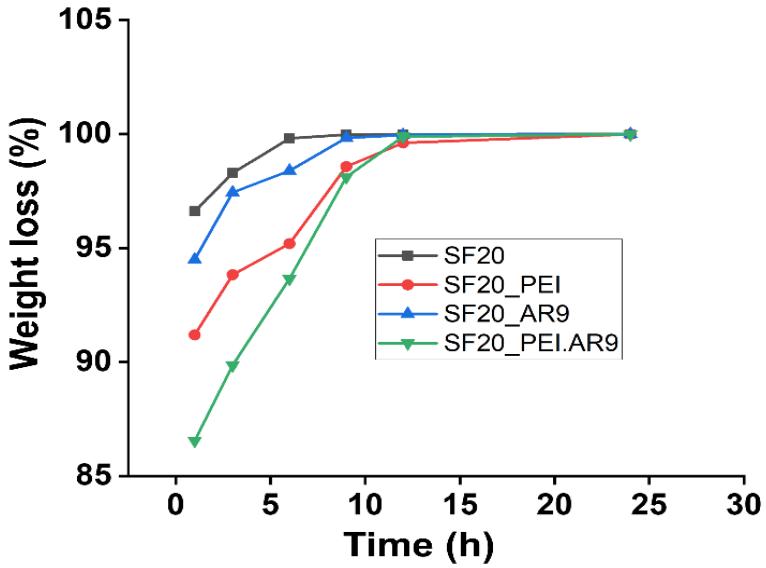

Figure 3. The degradation properties of the SF-based scaffolds after incubation in 0.1M NaOH.

Notably, the SF20_PEI.AR9 scaffold had the lowest degradation rate in sodium hydroxide solution at about 89.86% after 3 h incubation compared to other scaffolds all of which presented degradation rate above 93.84% within 3 h incubation (Fig.3). Moreover, under alkaline conditions, the SF proteins could have possibly been degraded through alkali hydrolysis of peptide bonds, resulting in the production of numerous amino acids with a low molecular weight, thus the observed reduction in the molecular weight of the silk fibroin scaffolds, in agreement with previous reports [33]. We speculate that the relatively slow rate of degradation of the polymerized scaffolds; SF20_PEI

Preprints (www.preprints.org) | NOT PEER-REVIEWED | Posted: 18 December 2023 doi:10.20944/preprints202312.1238.v1

and SF20_PEI.AR9 could be attributed to the dense network of bond interactions between the highly charged PEI and side chains of amino acids in SF.

2.5. Functional Groups Characterization by Raman and Fourier Infrared Spectroscopy

The SF scaffolds and the PEI polymerized SF scaffold samples, SF scaffolds incubated in bacteria or phages were tested by Fourier infrared spectroscopy and Raman spectroscopy to obtain the vibration spectrum of each sample. By calculating the intensity comparison parameters of different peak positions, the functional group characteristics can be analyzed to infer the secondary structure of the protein scaffold samples.

Figure 4 shows the FTIR spectra of the studied scaffolds and shows the vibration bands selected for the analysis of the scaffold structure.

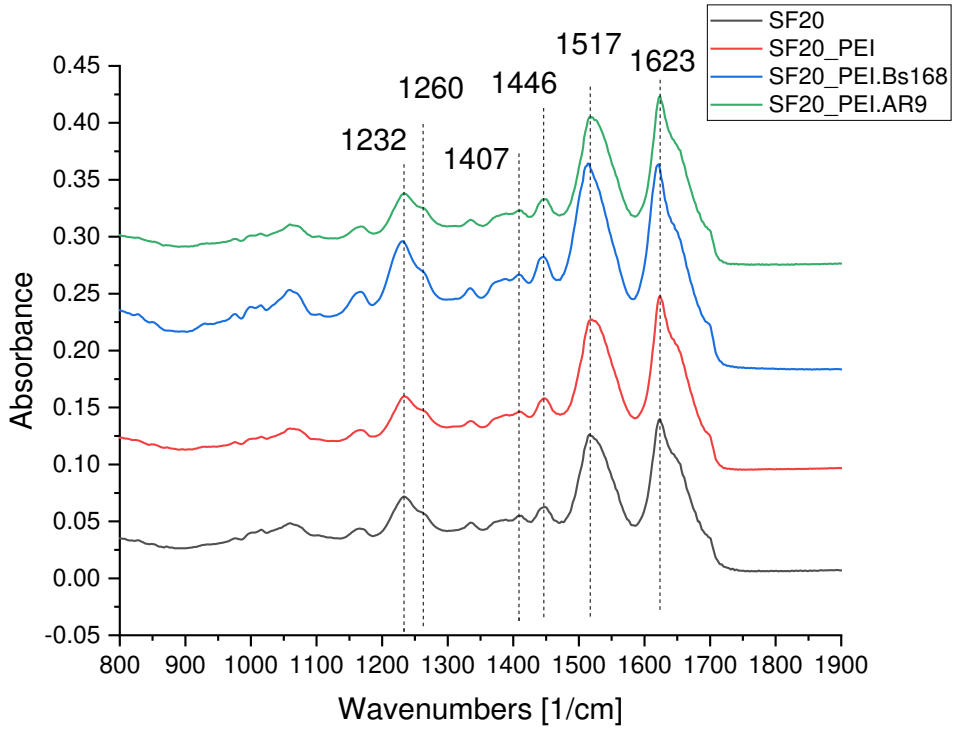

Figure 4. FTIR spectra of scaffolds (the averaged spectra are presented). .

As shown in the FTIR spectra of the scaffolds in Figure 4, the SF based scaffolds exhibited distinct peaks associated with group vibrations of the proteins Amide I at 1623 cm–1 corresponding of peptide bond vibrations mostly attributed to carbonyl group (C=O), the 1517 cm^{-1} band corresponding to group vibrations of Amide II peptide bonds, which include deformation and valence vibrations of N–H and C–N bonds, respectively [34-36], indicative of β-sheets present in SF [37]. Furthermore, Amid III band at 1232 cm–1 and 1260 cm^{-1} [34] also can be used to evaluate the secondary structure of proteins [38-40]. The band at 1446 cm–1 is usually referred to deformation vibrations of methylene groups in side chains of amino acids [41], while that at 1407 cm^{-1} corresponds to asymmetrical vibrations of COO- groups of amino acids [42-45]. The parameter I1407/I1446 allows for determination of the relative proportion of COO- residues, which is formed as a result of protein hydrolysis into individual amino acids [42]. Three assessed parameters which related to secondary structure of proteins - I1620/I1520, Amid II band position and I1232/I1260 showed an increase in the beta-sheets structures of the sample SF20_PEI.Bs168 based on parameter I1407/I1446, all groups except SF20_PEI.AR9 and SF20_PEI.Bs168 were significantly different with a P value, $p<0.05$.

In the IR spectrum of pure PEI, there is a sufficiently pronounced peak in the region of 1460 cm^{-1}, which could be observed in all samples containing PEI. The decrease in the parameter I1407/I1446

Preprints (www.preprints.org) | NOT PEER-REVIEWED | Posted: 18 December 2023 doi:10.20944/preprints202312.1238.v1

in the SF20_PEI sample compared to the pure SF sample was associated with the presence of PEI and not because of the destruction of the protein or the increase in COO- groups. However, an increase in the same parameter for SF20_PEI.AR9 and SF20_PEI.Bs168 samples compared to SF_PEI reflects an increase in the proportion of COO- groups, which may be due to partial hydrolysis of the protein.

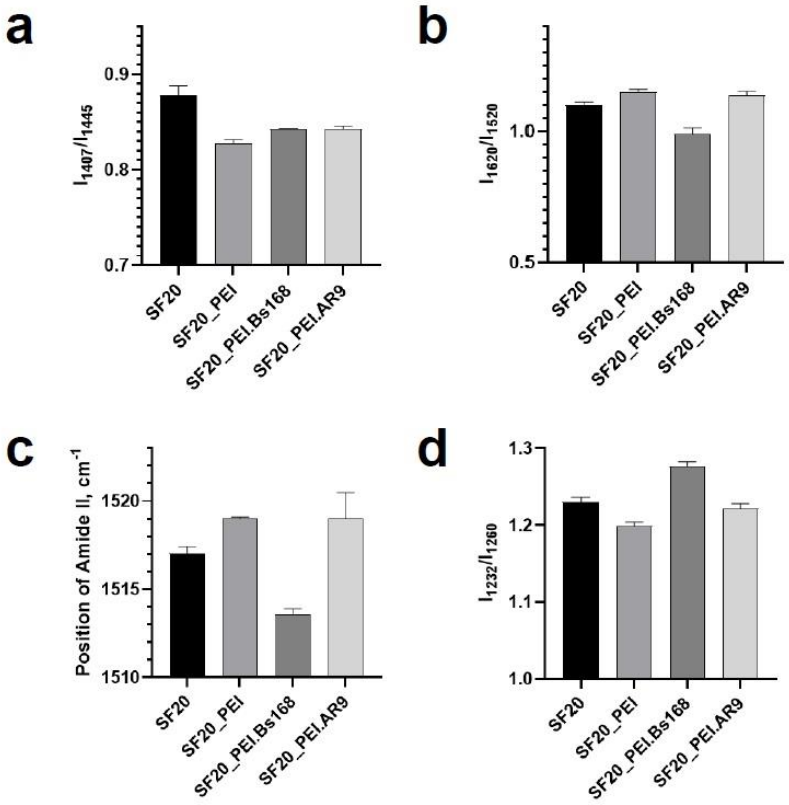

Figure 5. Functional groups characterization assessed by parameters a. I1407/I1446, b. I1620/I1520, c. position of Amide II , d. I1232/I1260 of FTIR spectra. All differences are statistically significant except difference between SF20_PEI.AR9 and SF20_PEI.Bs168, Student's test with P value, $p<0.05$.

Figure 6 shows the Raman spectra of the studied samples. They generally correspond to the spectra of silk fibroin.

There are 5,2 % of Tyr residues (277 residues of Tyr) in the sequenced parts of the repetitive H-fibroin region of *Bombix mori* silk fibroin [44]. Therefore, the lines of tyrosine residues are clearly distinguishable in the spectra of fibroin.

Preprints (www.preprints.org) | NOT PEER-REVIEWED | Posted: 18 December 2023 doi:10.20944/preprints202312.1238.v1

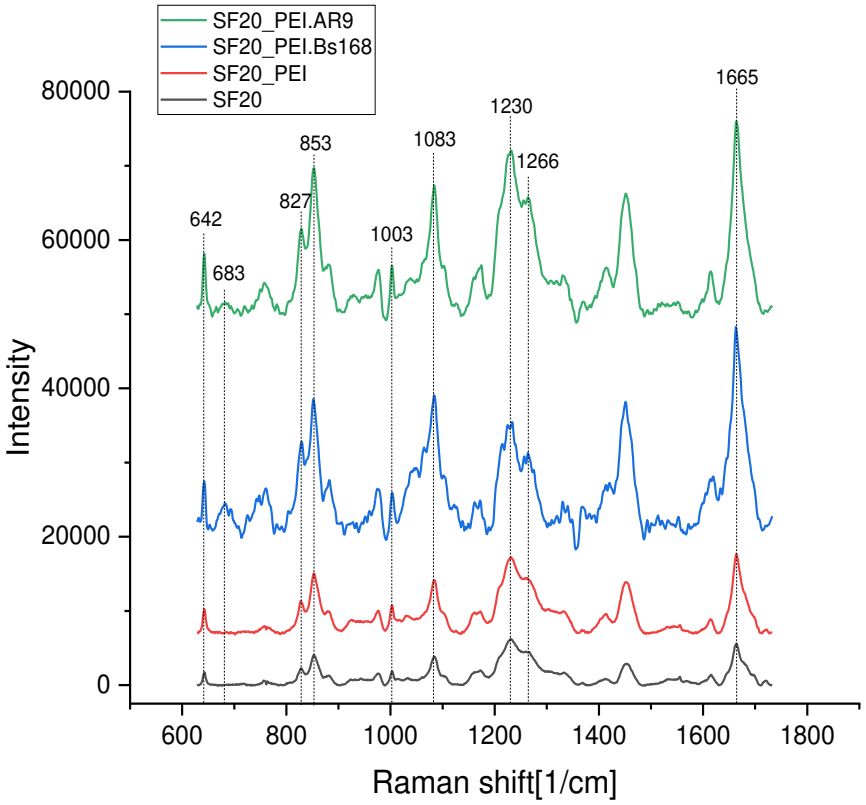

Figure 6. Raman spectra of scaffolds (the averaged spectra are presented).

A pair of Raman bands observed near 850 cm^{-1} and 830 cm^{-1} in proteins containing Tyr has been assigned to Fermi resonance between the in-plane breathing mode of the phenol ring (Y1 fundamental expected at 840 cm^{-1}) and an overtone of out-of-plane deformation mode (occurring near 420 cm^{-1}). It's an unambiguous marker of the hydrogen bonding state. The relative intensity ratio I850/I830 reflects the average of the hydrogen bonding states of all the tyrosines in protein containing more than one Tyr. I850/I830 ranges from 0.3 (phenolic OH is a strong hydrogen bond donor – "buried" tyrosine) to 2.5 (strong hydrogen acceptor – "exposed" tyrosine) [46,47].

Another band sensitive to changes in the structure of fibroin is 1083 cm^{-1}, associated with C-C fluctuations. According to the work [48,49], it is associated with the beta structure of the protein. The band 1003 cm^{-1} belongs to fluctuations in the aromatic ring of phenylalanine residues and is not affected by changes in structure [50]. Thus, the ratio of the intensities of the bands 1083 cm^{-1} and 1003 cm^{-1} can serve as an indicator of conformational changes in the protein. The bands in the region of 1230-1300 cm^{-1} belong to vibrations of Amide III, while peaks at low frequencies are characteristic of vibrations of amide bonds in beta structures [50]. A wide band in the region of 680 cm^{-1} may belong to vibrations of C-S bonds in cysteine and methionine residues [51,52].

The assessed parameters I850/I830 and I1230/I1266 in the studied samples were not different. However, the parameter I1083/I1003, which demonstrate a change in the secondary structure of the protein, significantly differed in the SF20_PEI.Bs168 sample, which indicated an increase in the proportion of beta structures in this sample and agrees with the data obtained by the FTIR method.

Parameter I683/I642 demonstrated an increase in C-S bond vibrations in SF20_PEI.Bs168 and SF20_PEI.AR9 samples. However, since fibroin contains very few residues of sulfur-containing amino acids [53], it is possible that this band showed the presence of bacterial or phage residues on the surface of scaffolds that have not been removed as a result of sample washing.

Preprints (www.preprints.org) | NOT PEER-REVIEWED | Posted: 18 December 2023 doi:10.20944/preprints202312.1238.v1

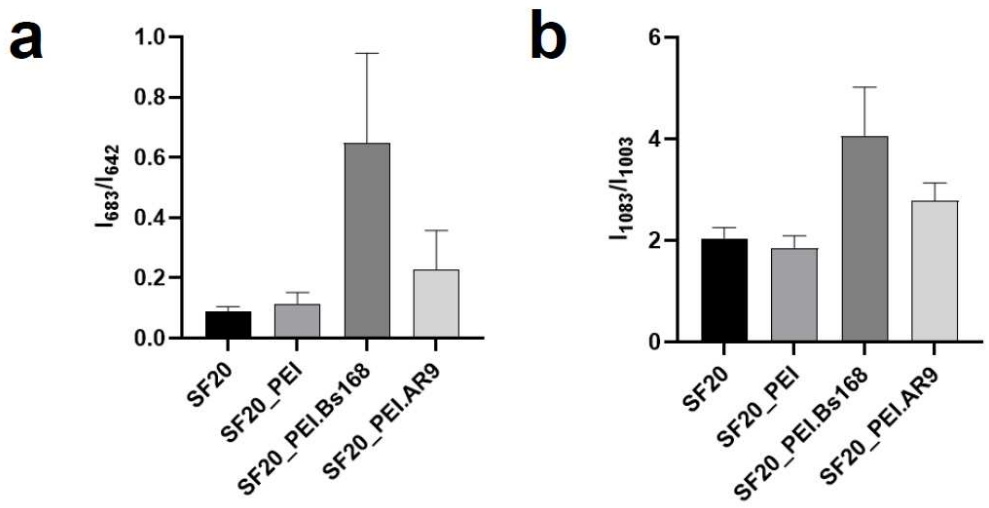

Figure 7. Functional groups characterization assessed by intensity parameters a. I683/I642, b. I1083/I1003 of Raman spectra. For the ratio I683/I642 SF20_PEI.Bs168 is statistically different from SF20 and SF20_PEI. For the ratio I1083/I1003 SF20_PEI.Bs168 and SF20_PEI.AR9 are statistically different from SF20 and SF20_PEI, Student's test with P value, $p<0.05$.

The protein structure may change during interaction with PEI, bacteria and phages. Partial protein degradation could be observed through the analysis of the spectra. It can also be found that the addition of bacteria and phages have an effect on the composition of the scaffolds.

2.6. The Antibacterial Activity of the SF- Phage Scaffolds

To determine the antibacterial potential of the SF based scaffolds, prior and after polymerization and functionalization with AR9 phages, Bacillus subtilis 168 cells were spread on LB agar petri dishes, then the scaffolds were placed on these plates and incubated at 37 °C, overnight. As shown in Fig. 8a, SEM micrographs revealed the differential effects of each composite scaffold. Comparatively, the PEI polymerized/ phage functionalized scaffold (SF20_PEI.AR9) scaffold exhibited the highest antibacterial activity with many visible dead cells on the surface (inset red arrows), while the phage functionalized non-polymerized SF20_AR9 scaffold also showed relative antimicrobial activity. The difference in the antibacterial activity of these two scaffolds could be related to the polymerization effect with PEI. As expected, PEI the polymerized scaffold possibly provided the surface positive charge that promoted interactions with the negatively charged phage capsid proteins [2]. These enhanced interactions facilitated phage immobilization at higher concentrations compared to the non-polymerized SF20-AR9 scaffold. Previous studies have also applied this polymerization approach for designing phage based scaffolds [54]. It should be noted here that our results further revealed the antibacterial effect of PEI on SF scaffolds as evidenced by several dead bacterial cells on the SF20_PEI scaffold. This could further open avenues for continued research on the antimicrobial mechanism of highly charged molecules like PEI. The SF20, control scaffold however had many live cells on its surface revealing its rather poor antibacterial effect (Fig. 8a Top left). This was further highlighted in the LB agar plates images in Fig. 8b (1-4) which showed that the PEI polymerized phage functionalized SF20_PEI.AR9 scaffold had the largest inhibition zone, confirming its high antibacterial potential compared to the other scaffolds.

Preprints (www.preprints.org) | NOT PEER-REVIEWED | Posted: 18 December 2023 doi:10.20944/preprints202312.1238.v1

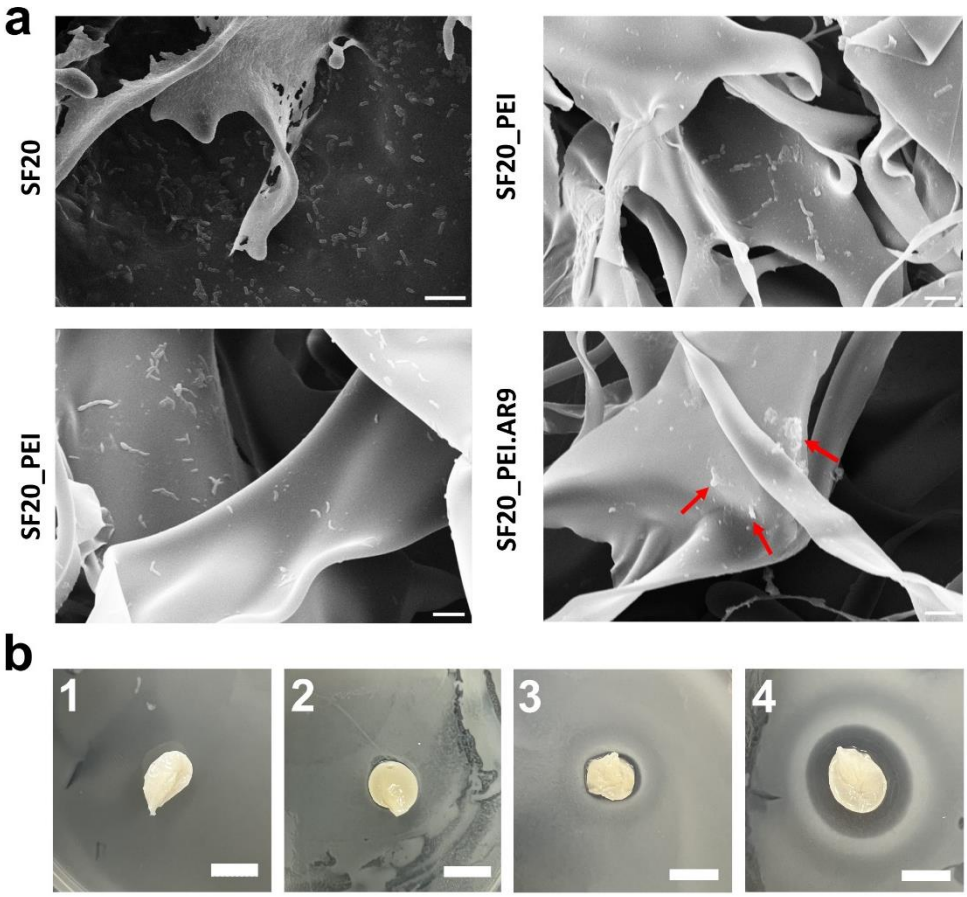

Figure 8. SEM micrographs of phage functionalized scaffolds and respective growth inhibition profiles. a. the antibacterial effect of SF20, SF20_PEI and phage functionalized SF20_AR9 and SF20_PEI.AR9 scaffolds. The red arrows show the dead bacterial cells on the SF20_PEI.AR9 scaffold; Bar size – 2 um; b. agar plates indicating the antimicrobial growth inhibition activity of the SF-based scaffolds; 1-4 represent SF20, SF20_PEI and phage functionalized SF20_AR9 and SF20_PEI.AR9 scaffolds, respectively. Bar – 10 mm.

3.8. Cell-Lysis/ Antibacterial Activity of the SF Phage Film

To elucidate further on the antibacterial effect of the phage functionalized scaffolds, we diluted the overnight cell cultures 100-fold, plated the diluent on LB agar plates, then placed the scaffolds on the surface. This was done to ensure low cell densities imitating either barely any infection or initial stages of infection. As shown in Fig. 9a, the PEI polymerized phage functionalized scaffold (SF20_PEI.AR9) showed a large clear zone of growth inhibition compared with the PEI polymerized scaffold without phages, thus highlighting the antibacterial effect of the phage functionalized scaffolds and potential application to prevent onset of infections. Measuring the zones of growth inhibition of the two scaffold types revealed a significant difference with the SF20_PEI.AR9 scaffold having a clear zone of approximately 78.3±7.6 mm compared to only 18.3±2.9 mm of the SF20_PEI scaffold without phages (Fig. 9b). Finally, we cultured cells on 50 ml conical flasks with composite scaffolds added while the controls were cells without scaffolds or phages (negative), and the positive control containing phage lysate only and OD600 taken in intervals. As shown in Fig. 9c, the lowest OD600 was observed on the flasks with only phages indicating the lytic effect of phages on bacterial cells. The flasks with SF20_PEI.AR9 scaffolds which were functionalized with AR9 phage after polymerizing with PEI had the second lowest OD600, further highlighting its antibacterial potential (Fig. 9c). The low growth rate could be attributed to the effect of the phages on bacterial growth, which could correlate with its antibacterial activity.

Preprints (www.preprints.org) | NOT PEER-REVIEWED | Posted: 18 December 2023 doi:10.20944/preprints202312.1238.v1

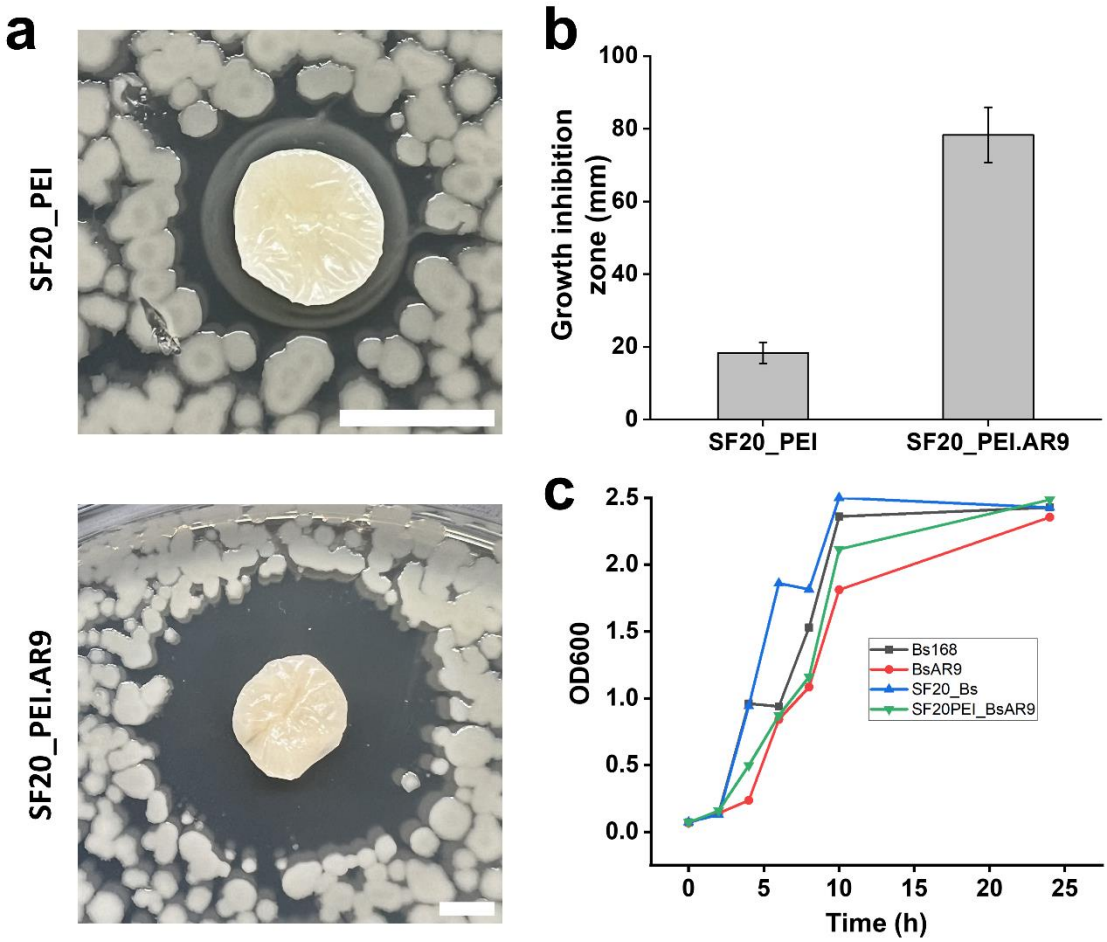

Figure 9. Cell lysis and growth curves of phage functionalized scaffolds. and respective growth inhibition profiles. a. the lytic/ growth inhibition zones of the polymerized scaffolds; SF20_PEI and phage functionalized SF20_PEI.AR9 scaffolds; Scale bar – 40 mm. b. size of the growth inhibition zones (mm) of the polymerized scaffolds; SF20_PEI and phage functionalized SF20_PEI.AR9 scaffolds. c. OD600 growth curves on flasks containing only bacterial cells (Bs 168) as negative control, BsAR9 flasks with both bacterial cells and AR9 phages added (positive control), SF20, flasks with the non-functionalized silk fibroin-based scaffold added and the SF20PEI_BsAR9 shows the growth curve of the phage functionalized PEI polymerized scaffold SF20_PEI.AR9.

3. Discussion

In the present study, to ensure effective immobilization of the bacteriophage on the SF-CS scaffold, such that the negatively charged phage capsid proteins bond with the substrate, polyethyleneimine was used. Polyethyleneimine is a structurally complex molecule characterized by a significant number of primary and secondary amine side groups, was used to polymerize the scaffold, with the aim of introducing positive charges on scaffold surface which can foster interactions with the phage capsid allowing the tail fibres to freely associate with bacteria. Furthermore, the presence of several branched groups in polyethyleneimine can potentially facilitate the development of intricate structures with SF-CS scaffold, hence enhancing the physiochemical properties of the scaffold with respect to intended applications.

Polymerization with the silk fibroin induced formation of a positively charged scaffold, which would further facilitate electrostatic interactions with the negatively charged phage head proteins, leaving free the phage tails, which are a specialized nanomachinery capable of identifying bacterial host wall and/or membrane, and release the phage genome into the host cytosol in order to generate new viral particles.

 doi:10.20944/preprints202312.1238.v1

Based on the cell lysis/ antimicrobial assay experiments conducted, the growth inhibition zones of the PEI polymerized SF20_PEI scaffold and phage functionalized SF20_PEI.AR9 scaffold were found to be 18.3± 2.9 mm and 78.3± 7.6 mm, respectively. The results indicated the antibacterial activity of the scaffolds and specifically highlighted the significant lytic potential of the phages on bacterial host cells, thus fulfilling the objective of the study. Moreover, the alteration processes of the SF based scaffold with PEI was also accompanied by notable improvement in the physiochemical characteristics of the scaffold. For example, the degradation rate of the SF20_PEI.AR9 scaffold was lower than the other scaffolds in the study hence showing potential for long term applications in tissue engineering.

In addition, structural and functional group properties of SF based scaffolds were analyzed using spectral and analytical techniques such as FT-IR, and Raman spectroscopy. We demonstrated an increase in the beta-sheets structures of the sample SF20_PEI.Bs168, which can be considered as a change in fibroin structure. The increase of the free amino acids in SF20_PEI.Bs168 and SF20_PEI.AR9 scaffolds may be the evidence of partially degradation of fibroin in this samples. The increase in C-S bond vibrations in SF20_PEI.Bs168 and SF20_PEI.AR9 samples can show the presence of bacterial or phage residues.

Based on the growth inhibition profiles of the functionalized scaffold, it could be deduced that the scaffold is more suitable for application as a preventive measure against bacterial infections in wounds. In the future, this model system can be applied to the pathogenic bacteria, like *P. aeruginosa* and giant phages PhiKZ, infective towards it.

4. Materials and Methods

4.1. Bacterial Culture and Phage Propagation

LAMME Wuxi (China), kindly provided Bacillus subtilis 168, the phage's host strain. The strain was cultured in LB medium overnight at 37℃, at 200rpm, then expanded in 100 mL medium as previously reported [55], and further cultured under the same conditions for 3-4 h until an OD600 of approximately 0.7-0.8 is achieved. Diluted AR9 phage is then added into the exponential phase host strain, and cultured in shake flasks at 37℃, at 200rpm for 8h. The phage lysate is collected by centrifuging the cultured cells at 30,000 g for 30 minutes prior to sterile filtration in a 0.22 μm membrane followed by storage at 4℃, for further experiments.

4.2. Regeneration of Silk Fibroin (SF)

Silk fibroin (SF) solution regeneration and the composite phage films were prepared following a previously reported protocol with slight modifications [2,56]. Briefly, 6 g of SF was submerged in a 1:8:2 molar ratio solution of calcium chloride, water and ethanol then placed in a water bath at 85℃ for 6 h. The dissolved SF solution was left to cool to room temperature before dialysis in ultra-pure water for 3 days. The SF solution was then centrifuged and diluted to a concentration of 20 mg/mL stock solution.

4.3. Preparation of SF- Bacteriophage Composite Scaffolds

To prepare the SF based scaffold, the stock solution (20mg/ml) was thoroughly mixed with 1% DMSO, spread on 48 well plates then cooled at -80 ℃ for 5 days prior to future use. The prepared SF composites were gradually thawed in ethanol and washed with distilled water to remove the freely adsorbed ethanol. Thereafter, the SF- scaffolds were polymerized with Polyethyleneimine (PEI) following a previously reported protocol with minor modifications [57]. Briefly, the SF composites were suspended in 5 wt% PEI solution, and the pH was adjusted to 7 using 0.1 M HCl. Further, 0.21 wt% sodium cyanoborohydride was added to the reaction mixture to accelerate the polymerization in a sonicator for 1 h. The prepared composites were referred to as SF20, SF20_PEI for the non-polymerized and polymerized SF scaffolds, respectively.

To develop the phage functionalized scaffolds, the SF20 and polymerized SF20Pei were submerged in a phage lysate with predetermined multiplicity of infection of 1 and incubated at 25 ℃

Preprints (www.preprints.org) | NOT PEER-REVIEWED | Posted: 18 December 2023 doi:10.20944/preprints202312.1238.v1

for 2 h, then transferred to 4 ℃, overnight, prior to washing with deionized water, dehydration and application for the assays. The prepared AR9 phage functionalized composites were referred to as SF20_AR9 and SF20_PEI.AR9 for the non-polymerized phage functionalized and polymerized phage functionalized SF scaffolds, respectively.

4.4. Scaffold Morphological, and Functional Groups Characterization

4.4.1. Scanning Electron Microscopy (SEM) Testing

The scaffold samples were frozen at -80℃ for 10 min, then were subjected to lyophilization overnight in LABCONCO 4.5l lyophilizer (USA). The samples were to a metal substrate using the carbon double-sided tape and sputter-coated for 70s in Ar atmosphere with gold in KYKY SBC-12 ion sputter coater (China) apparatus. SEM mages were obtained in a KYKY EM6200 SEM (China) at x100, x200, x1000 magnification. The images were edited using GIMP 2.12 software.

4.4.2. Fourier Transform Infrared Spectroscopy

The Fourier transform infrared (FTIR) spectra were measured using a FTIR spectroscopy (iCAN 9, Tianjing Nengpu, China) in attenuated total reflectance (ATR) mode. The 3 independent spectra were measured on a sample and averaged. All spectra were analyzed using SpectraGryph 1.2 and Origin 2021 software.

4.4.3. Raman Spectroscopy

The Raman spectra were recorded using a confocal Raman spectrometer (InVia, Renishaw Plc. Wotton-under-Edge, Gloucestershire, UK) equipped with a Leica DM2700M microscope system, a 780 nm (50 mW) excitation laser source and a 1200 l/mm grating. For each single point of sample, at least 3 spectra were acquired in static scan mode ranging from 700 to 1800 cm^{-1}. Spectral manipulations were performed using WiRE 5.2 for baseline subtraction, SpectraGryph 1.2 for average, and Origin 2021 for drawing figures.

4.5. In Vitro Swelling Rate and Water Solubility Determination of the Scaffolds

The determination of the swelling rate *in vitro* was conducted using the methodology described by Jin et al. [58], with some adjustments. The samples were partitioned into splines with a circumference of approximately 10 mm. Each was accurately measured, submerged in a phosphate-buffered saline (PBS) solution at pH 7.4, and then carefully maintained at 37°C. Subsequently, the samples underwent different durations of exposure, spanning from 0 minutes to 14 days, during which changes in weight and diameter were closely observed as indicators of fluid absorption and swelling. The duration of the observation period extended until the samples hit a threshold at which their mass no longer exhibited any further rise. Surface moisture was removed from the samples using Kimwipes. Afterwards, the wet weight of the sample (referred to as Ws) was ascertained, and measurements were collected for both the head and thread diameters. The determination of the swelling rate of the membrane is calculated via Equation (1).

$$E_{SR}/\% = \frac{m_t - m_o}{m_o} \times 100 \quad (1)$$

Formula: ESR, scaffold swelling rate, %; mo, initial mass of scaffold, mg; mt, mass after swelling of the scaffold, mg.

For water solubility (WS %) determination, dry scaffold samples were cut into uniform measurements and processed. The water solubility was then determined by transferring it to a centrifuge tube containing 25 mL of sterile ultrapure water. The samples were placed in a shaker a shaker at 37 degrees and 150 revolutions per minute for a duration of 24 hours. Undissolved fragments were recovered by centrifugation at a speed of 30,000 g at a temperature of 4 °C for 20 minutes. To acquire the dried undissolved scaffold material, place the fragments in a drying oven at

 doi:10.20944/preprints202312.1238.v1

a temperature of 50 °C for a duration of 24 hours, then precisely measure the mass. Equation (2) demonstrates the computation of the water solubility of the scaffolds. The calculation of the water solubility of the membrane is shown in Equation (2):

$$WS/\% = \frac{m_i - m_f}{m_i} \times 100 \quad (2)$$

Here, WS is the water solubility, %; mi, initial mass of scaffold, mg; mf, dry and undissolved scaffold mass after dissolution in water, mg

4.6. In Vitro Degradation Test

To investigate the degradation of silk fibroin-based scaffolds in an in vitro setting, a total of three machined silk bone screws were subjected to different processing conditions. These scaffolds were incubated at a temperature of 37 °C in 0.1 M sodium hydroxide, and phosphate-buffered saline (PBS) solution pH 7.4. A volume of 2 mL of incubation solution was utilized for each SF scaffold. The incubation solutions (specifically PBS) was replaced at intervals of 2-3 days. Samples were cleaned in deionized water and dried before being weighed at specific time intervals (1 day, 3 days, 6 days, 9 days, 12 days and 24 days). Following uninterrupted incubation period, the samples underwent a rinsing process using deionized water and were subsequently dried prior to being weighed. The recorded and processed data consisted of the remaining mass of each sample and the dried samples were used for Raman spectroscopy and Fourier infrared spectroscopy analysis.

4.7. Plaque Assay of SF- Based Immobilized Phage Composites

The approach suggested [2] underwent minor modifications. Based on this, the scaffold designated for analysis was divided into circular samples with a diameter of 10 mm and underwent a sterilization procedure utilizing UV radiation for a duration of 15 minutes. A solution of *Bacillus subtilis* 168 with a concentration of approximately 10 colony-forming units per milliliter (CFU/mL) was uniformly distributed onto the pre-solidified LB agar medium using a 100 μL volume. Subsequently, the medium that had been coated was left undisturbed for a period of 20 minutes. The circular membrane specimen should be placed onto a stable substrate and exposed to a controlled environment at a temperature of 37 °C for a period of 24 hours. The measurement of the inhibition diameter and the documentation of colony forming units on agar plates was done through photography.

4.8. Cell-Lysis/ Antibacterial Activity of the SF Phage Film

Different kinds of scaffolds were put into concentrated phage lysate in room temperature for 2 hrs to promote phages attach scaffolds, then keep them in 4℃ overnight. Then pick out scaffolds from the phage lysate and wash them 1 time with 0.01 M phosphate-buffered saline (PBS) to wash out the phages unattached. Scaffolds with and without phage treatment were separately put into 3 ml BS168 LB medium (OD600=0.8-0.9) for interaction. The scaffolds were taken out after 2 hrs and washed by PBS again. The process of SEM test is the same as 2.8.

100 ul BS168 LB medium (OD600=0.8-0.9) were put into 10 ml sterile LB medium. Then induce 100 ul phage lysate, non-treated SF20 scaffold, phage-treated SF20_PEI scaffold separately into each sample, and cultured in shake flasks at 37℃, 200rpm. OD600 values were checked after 0, 2, 4, 6, 8, 10, 24 hrs.

3 ul BS168 LB medium (OD600=0.8-0.9) were injected into 1.5% agar LB solid medium in petri dish and cultured in incubator with 37℃ for 2 d. SF20 and SF20_PEI scaffolds were onto solid bacteria biofilm and cultured in incubator with 37℃ for 2d again. Then observed the growth of bacteria.

Author Contributions: Conceptualization, X.X. and Y.Y.; methodology, X.X.; software, X.X.; validation, X.X., Y.Y. and Z.Z.; formal analysis, X.X.; investigation, X.X.; resources, X.X.; data curation, X.X.; writing—original draft preparation, X.X.; writing—review and editing, X.X.; visualization, X.X.; supervision, X.X.; project

administration, X.X.; funding acquisition, Y.Y. All authors have read and agreed to the published version of the manuscript.

Funding: This study was supported by Innovation Committee of Science and Technology of Shenzhen City, PRC. Grant No. 20200828172651001 to OSS.

Acknowledgments: Authors thank Dr. A. Arkhipova for fruitful discussions and providing the basic methodology for the preparation of scaffolds. YW and GL acknowledge Shenzhen Municipal Government and Shenzhen MSU-BIT University support.

Conflicts of Interest: The authors declare no conflict of interest.

References

1. Luckanagul, J.; Lee, L.A.; Nguyen, Q.L.; Sitasuwan, P.; Yang, X.M.; Shazly, T.; Wang, Q. Porous Alginate Hydrogel Functionalized with Virus as Three-Dimensional Scaffolds for Bone Differentiation. *Biomacromolecules* **2012**, *13*, 3949-3958, doi:10.1021/bm301180c.
2. Farooq, U.; Ullah, M.W.; Yang, Q.; Aziz, A.; Xu, J.; Zhou, L.; Wang, S. High-density phage particles immobilization in surface-modified bacterial cellulose for ultra-sensitive and selective electrochemical detection of Staphylococcus aureus. *Biosens Bioelectron* **2020**, *157*, 112163, doi:10.1016/j.bios.2020.112163.
3. Bichara, D.A.; Zhao, X.; Bodugoz-Senturk, H.; Ballyns, F.P.; Oral, E.; Randolph, M.A.; Bonassar, L.J.; Gill, T.J.; Muratoglu, O.K. Porous poly(vinyl alcohol)-hydrogel matrix-engineered biosynthetic cartilage. *Tissue Eng Part A* **2011**, *17*, 301-309, doi:10.1089/ten.TEA.2010.0322.
4. Adams, B.L.; Hurley, M.M.; Jahnke, J.P.; Stratis-Cullum, D.N. Functional and Selective Bacterial Interfaces Using Cross-Scaffold Gold Binding Peptides. *Jom-Us* **2015**, *67*, 2483-2493, doi:10.1007/s11837-015-1662-7.
5. Scharff, R.L. Food Attribution and Economic Cost Estimates for Meat- and Poultry-Related Illnesses. *Journal of food protection* **2020**, *83*, 959-967, doi:10.4315/jfp-19-548.
6. Cámara, M.; Green, W.; MacPhee, C.E.; Rakowska, P.D.; Raval, R.; Richardson, M.C.; Slater-Jefferies, J.; Steventon, K.; Webb, J.S. Economic significance of biofilms: a multidisciplinary and cross-sectoral challenge. *npj Biofilms and Microbiomes* **2022**, *8*, 42, doi:10.1038/s41522-022-00306-y.
7. Li, M.; Zhang, Z.; Liang, Y.; He, J.; Guo, B. Multifunctional Tissue-Adhesive Cryogel Wound Dressing for Rapid Nonpressing Surface Hemorrhage and Wound Repair. *ACS Applied Materials & Interfaces* **2020**, *12*, 35856-35872, doi:10.1021/acsami.0c08285.
8. Rather, M.A.; Gupta, K.; Mandal, M. Microbial biofilm: formation, architecture, antibiotic resistance, and control strategies. *Brazilian journal of microbiology : [publication of the Brazilian Society for Microbiology]* **2021**, *52*, 1701-1718, doi:10.1007/s42770-021-00624-x.
9. Ventola, C.L. The antibiotic resistance crisis: part 1: causes and threats. *P & T : a peer-reviewed journal for formulary management* **2015**, *40*, 277-283.
10. Guo, Q.; Han, J.J.; Shan, S.; Liu, D.F.; Wu, S.S.; Xiong, Y.H.; Lai, W.H. DNA-based hybridization chain reaction and biotin-streptavidin signal amplification for sensitive detection of Escherichia coli O157:H7 through ELISA. *Biosens Bioelectron* **2016**, *86*, 990-995, doi:10.1016/j.bios.2016.07.049.
11. Hao, Y.; Zhang, Y.; Mensah, A.; Liao, S.; Lv, P.; Wei, Q. Scalable, ultra-high stretchable and conductive fiber triboelectric nanogenerator for biomechanical sensing. *Nano Energy* **2023**, *109*, 108291, doi:https://doi.org/10.1016/j.nanoen.2023.108291.
12. Mensah, A.; Yajun, C.; Asinyo, B.K.; Howard, E.K.; Huang, J.; Narh, C.; Wei, Q. Singlet oxygen (1O2) induced photodynamic inactivation of bacterials with bioactive Icariin/beta-cyclodextrin/bacterial cellulose. *Polymer Testing* **2022**, *112*, 107600, doi:https://doi.org/10.1016/j.polymertesting.2022.107600.
13. Asif, M.; Aziz, A.; Azeem, M.; Wang, Z.; Ashraf, G.; Xiao, F.; Chen, X.; Liu, H. A review on electrochemical biosensing platform based on layered double hydroxides for small molecule biomarkers determination. *Advances in Colloid and Interface Science* **2018**, *262*, 21-38, doi:https://doi.org/10.1016/j.cis.2018.11.001.
14. Li, W.; Separovic, F.; O'Brien-Simpson, N.M.; Wade, J.D. Chemically modified and conjugated antimicrobial peptides against superbugs. *Chemical Society Reviews* **2021**, *50*, 4932-4973, doi:10.1039/D0CS01026J.
15. Wu, L.; Song, Y.; Luan, T.; Ma, L.; Su, L.; Wang, S.; Yan, X. Specific detection of live Escherichia coli O157:H7 using tetracysteine-tagged PP01 bacteriophage. *Biosens Bioelectron* **2016**, *86*, 102-108, doi:10.1016/j.bios.2016.06.041.
16. Amankwah, S.; Abdella, K.; Kassa, T. Bacterial Biofilm Destruction: A Focused Review On The Recent Use of Phage-Based Strategies With Other Antibiofilm Agents. *Nanotechnology, science and applications* **2021**, *14*, 161-177, doi:10.2147/nsa.S325594.

17. Richter, Ł.; Księżarczyk, K.; Paszkowska, K.; Janczuk-Richter, M.; Niedziółka-Jönsson, J.; Gapiński, J.; Łoś, M.; Hołyst, R.; Paczesny, J. Adsorption of bacteriophages on polypropylene labware affects the reproducibility of phage research. *Sci Rep-Uk* **2021**, *11*, 7387, doi:10.1038/s41598-021-86571-x.
18. Mojtabavi, M.; Greive, S.J.; Antson, A.A.; Wanunu, M. High-Voltage Biomolecular Sensing Using a Bacteriophage Portal Protein Covalently Immobilized within a Solid-State Nanopore. *J Am Chem Soc* **2022**, *144*, 22540-22548, doi:10.1021/jacs.2c08514.
19. Choi, I.; Yoo, D.S.; Chang, Y.; Kim, S.Y.; Han, J. Polycaprolactone film functionalized with bacteriophage T4 promotes antibacterial activity of food packaging toward Escherichia coli. *Food Chem* **2021**, *346*, 128883, doi:10.1016/j.foodchem.2020.128883.
20. Yehl, K.; Lemire, S.; Yang, A.C.; Ando, H.; Mimee, M.; Torres, M.T.; de la Fuente-Nunez, C.; Lu, T.K. Engineering Phage Host-Range and Suppressing Bacterial Resistance through Phage Tail Fiber Mutagenesis. *Cell* **2019**, *179*, 459-469.e459, doi:10.1016/j.cell.2019.09.015.
21. Kopač, T.; Lisac, A.; Mravljak, R.; Ručigaj, A.; Krajnc, M.; Podgornik, A. Bacteriophage Delivery Systems Based on Composite PolyHIPE/Nanocellulose Hydrogel Particles. **2021**, *13*, 2648.
22. Douglas, T.; Wang, Y. Bioinspired Approaches to Self-Assembly of Virus-like Particles: From Molecules to Materials. *Accounts Chem Res* **2022**, *55*, 1349-1359, doi:10.1021/acs.accounts.2c00056.
23. Laughlin, T.G.; Deep, A.; Prichard, A.M.; Seitz, C.; Gu, Y.J.; Enustun, E.; Suslov, S.; Khanna, K.; Birkholz, E.A.; Armbruster, E.; et al. Architecture and self-assembly of the jumbo bacteriophage nuclear shell. *Nature* **2022**, *608*, 429-+, doi:10.1038/s41586-022-05013-4.
24. Roy, M.D.; Stanley, S.K.; Amis, E.J.; Becker, M.L.J.A.M. Identification of a highly specific hydroxyapatite-binding peptide using phage display. **2008**, *20*, 1830-1836.
25. Jin, L.; Cao, F.; Gao, Y.; Zhang, C.; Qian, Z.; Zhang, J.; Mao, Z.J.A.M. Microenvironment Activated Nanozymes-Armed Bacteriophages Efficiently Combat Bacterial Infection. **2023**, 2301349.
26. Singh, A.; Glass, N.; Tolba, M.; Brovko, L.; Griffiths, M.; Evoy, S.J.B.; Bioelectronics. Immobilization of bacteriophages on gold surfaces for the specific capture of pathogens. **2009**, *24*, 3645-3651.
27. Konwarh, R.; Karak, N.; Misra, M.J.B.a. Electrospun cellulose acetate nanofibers: the present status and gamut of biotechnological applications. **2013**, *31*, 421-437.
28. Peifen, M.; Mengyun, L.; Jinglong, H.; Danqian, L.; Yan, T.; Liwei, X.; Han, Z.; Jianlong, D.; Lingyan, L.; Guanghui, Z.J.B.; et al. New skin tissue engineering scaffold with sulfated silk fibroin/chitosan/hydroxyapatite and its application. **2023**, *640*, 117-124.
29. Eivazzadeh-Keihan, R.; Radinekiyan, F.; Aliabadi, H.A.M.; Sukhtezari, S.; Tahmasebi, B.; Maleki, A.; Madanchi, H.J.S.r. Chitosan hydrogel/silk fibroin/Mg (OH) 2 nanobiocomposite as a novel scaffold with antimicrobial activity and improved mechanical properties. **2021**, *11*, 650.
30. do Nascimento, M.H.M.; Ferreira, M.; Malmonge, S.M.; Lombello, C.B. Evaluation of cell interaction with polymeric biomaterials based on hyaluronic acid and chitosan. *Journal of Materials Science: Materials in Medicine* **2017**, *28*, 68, doi:10.1007/s10856-017-5875-x.
31. Tajvar, S.; Hadjizadeh, A.; Samandari, S.S.J.I.B.; Biodegradation. Scaffold degradation in bone tissue engineering: An overview. **2023**, *180*, 105599.
32. Sung, H.-J.; Meredith, C.; Johnson, C.; Galis, Z.S.J.B. The effect of scaffold degradation rate on three-dimensional cell growth and angiogenesis. **2004**, *25*, 5735-5742.
33. Chao, M.; He, L.; Gong, M.; Li, N.; Li, X.; Peng, L.; Shi, F.; Zhang, L.; Wan, P.J.A.n. Breathable Ti3C2T x MXene/Protein Nanocomposites for Ultrasensitive Medical Pressure Sensor with Degradability in Solvents. **2021**, *15*, 9746-9758.
34. Hong, H.; Lee, O.J.; Lee, Y.J.; Lee, J.S.; Ajiteru, O.; Lee, H.; Suh, Y.J.; Sultan, M.T.; Kim, S.H.; Park, C.H.J.B. Cytocompatibility of modified silk fibroin with glycidyl methacrylate for tissue engineering and biomedical applications. **2020**, *11*, 35.
35. Lorenz-Fonfria, V.A.J.C.r. Infrared difference spectroscopy of proteins: from bands to bonds. **2020**, *120*, 3466-3576.
36. Wen, Z.; Xin, C.; Zhengzhong, S.J.P.i.C. Conformation studies of silk proteins with infrared and raman spectroscopy. **2006**, *18*, 1514.
37. Kalnin, N.N.; Baikalov, I.A.; Venyaminov, S. Quantitative IR spectrophotometry of peptide compounds in water (H2O) solutions. III. Estimation of the protein secondary structure. *Biopolymers* **1990**, *30*, 1273-1280, doi:10.1002/bip.360301311.
38. Cai, S.W.; Singh, B.R. A distinct utility of the amide III infrared band for secondary structure estimation of aqueous protein solutions using partial least squares methods. *Biochemistry* **2004**, *43*, 2541-2549, doi:10.1021/bi030149y.
39. Singh, B.; DeOliveira, D.; Fu, F.-N.; Fuller, M. *Fourier transform infrared analysis of amide III bands of proteins for the secondary structure estimation*; SPIE: 1993; Volume 1890.

40. Stani, C.; Vaccari, L.; Mitri, E.; Birarda, G. FTIR investigation of the secondary structure of type I collagen: New insight into the amide III band. *Spectrochim Acta A* **2020**, *229*, doi:ARTN 11800610.1016/j.saa.2019.118006.
41. Dongmei, W.; Jinli, C.; ZHANG, Y.J.S.; Analysis, S. The structure characterization of polyethylenimine vis FTIR. **2016**, *36*, 199-200.
42. Barth, A. Infrared spectroscopy of proteins. *Biochimica et Biophysica Acta (BBA) - Bioenergetics* **2007**, *1767*, 1073-1101, doi:https://doi.org/10.1016/j.bbabio.2007.06.004.
43. Kristoffersen, K.A.; van Amerongen, A.; Böcker, U.; Lindberg, D.; Wubshet, S.G.; de Vogel-van den Bosch, H.; Horn, S.J.; Afseth, N.K. Fourier-transform infrared spectroscopy for monitoring proteolytic reactions using dry-films treated with trifluoroacetic acid. *Sci Rep-Uk* **2020**, *10*, 7844, doi:10.1038/s41598-020-64583-3.
44. Fedič, R.; Žurovec, M.; Sehnal, F. Correlation between Fibroin Amino Acid Sequence and Physical Silk Properties*. *Journal of Biological Chemistry* **2003**, *278*, 35255-35264, doi:https://doi.org/10.1074/jbc.M305304200.
45. Böcker, U.; Wubshet, S.G.; Lindberg, D.; Afseth, N.K. Fourier-transform infrared spectroscopy for characterization of protein chain reductions in enzymatic reactions. *The Analyst* **2017**, *142*, 2812-2818, doi:10.1039/c7an00488e.
46. Le Bihan, T.; Blochet, J.-É.; Désormeaux, A.; Marion, D.; Pézolet, M. Determination of the Secondary Structure and Conformation of Puroindolines by Infrared and Raman Spectroscopy. *Biochemistry* **1996**, *35*, 12712-12722, doi:10.1021/bi960869n.
47. Zhang, Z.; Yang, Y.; Tang, X.; Chen, Y.; You, Y. Chemical forces study of heat-induced myofibrillar protein gel as affected by partial substitution of NaCl with KCl, MgCl2 and CaCl2. *CyTA - Journal of Food* **2016**, *14*, 239-247, doi:10.1080/19476337.2015.1091038.
48. Monti, P.; Freddi, G.; Tsukada, M.; Bertoluzza, A.; Asakura, T. Spectroscopic characterization of Bombyx mori silk fibroin: Raman spectrum of Silk I. In *Spectroscopy of Biological Molecules: New Directions: 8th European Conference on the Spectroscopy of Biological Molecules, 29 August–2 September 1999, Enschede, The Netherlands*, Greve, J., Puppels, G.J., Otto, C., Eds.; Springer Netherlands: Dordrecht, 1999; pp. 81-82.
49. Lefèvre, T.; Paquet-Mercier, F.; Lesage, S.; Rousseau, M.-E.; Bédard, S.; Pézolet, M. Study by Raman spectromicroscopy of the effect of tensile deformation on the molecular structure of Bombyx mori silk. *Vibrational Spectroscopy* **2009**, *51*, 136-141, doi:https://doi.org/10.1016/j.vibspec.2008.11.012.
50. Ryguła, A.; Majzner, K.; Marzec, K.M.; Kaczor, A.; Pilarczyk, M.; Barańska, M.J.J.o.R.S. Raman spectroscopy of proteins: a review. **2013**, *44*, 1061-1076.
51. Bazylewski, P.; Divigalpitiya, R.; Fanchini, G. In situ Raman spectroscopy distinguishes between reversible and irreversible thiol modifications in l-cysteine. *Rsc Adv* **2017**, *7*, 2964-2970, doi:10.1039/C6RA25879D.
52. Kocherbitov, V.; Latynis, J.; Misiūnas, A.; Barauskas, J.; Niaura, G. Hydration of Lysozyme Studied by Raman Spectroscopy. *The Journal of Physical Chemistry B* **2013**, *117*, 4981-4992, doi:10.1021/jp4017954.
53. Robson, A.; Woodhouse, J.M.; Zaidi, Z.H. Cystine in silk fibroin, Bombyx mori. *Int J Protein Res* **1970**, *2*, 181-189, doi:10.1111/j.1399-3011.1970.tb01676.x.
54. Vonasek, E.; Lu, P.; Hsieh, Y.-L.; Nitin, N. Bacteriophages immobilized on electrospun cellulose microfibers by non-specific adsorption, protein–ligand binding, and electrostatic interactions. *Cellulose* **2017**, *24*, 4581-4589, doi:10.1007/s10570-017-1442-3.
55. Romero, D.; Aguilar, C.; Losick, R.; Kolter, R.J.P.o.t.N.A.o.S. Amyloid fibers provide structural integrity to Bacillus subtilis biofilms. **2010**, *107*, 2230-2234.
56. Ajisawa, A.J.T.J.o.S.S.o.J. Dissolution of silk fibroin with calciumchloride/ethanol aqueous solution Studies on the dissolution of silk fibroin.(IX). **1998**, *67*, 91-94.
57. Li, C.; Zhang, M.; Liu, S.-Y.; Zhang, F.-S.; Wan, T.; Ding, Z.-T.; Zhang, P.-X.J.P. Chitin nerve conduits with three-dimensional spheroids of mesenchymal stem cells from sd rats promote peripheral nerve regeneration. **2021**, *13*, 3957.
58. Jin, X.; Xiang, Z.; Liu, Q.; Chen, Y.; Lu, F.J.B.t. Polyethyleneimine-bacterial cellulose bioadsorbent for effective removal of copper and lead ions from aqueous solution. **2017**, *244*, 844-849.